Kubo et al. Earth, Planets and Space (2016) 68:16
DOI 10.1186/s40623-016-0393-5

Earth, Planets and Space
a SpringerOpen Journal

LETTER Open Access

# Estimation of the source process of the 2015 Gorkha, Nepal, earthquake and simulation of long-period ground motions in the Kathmandu basin using a one-dimensional basin structure model

Hisahiko Kubo*, Yadab P. Dhakal, Wataru Suzuki, Takashi Kunugi, Shin Aoi and Hiroyuki Fujiwara

**Abstract**

The source rupture process of the 2015 Gorkha, Nepal, earthquake was estimated by the joint kinematic source inversion with near-field waveforms, teleseismic waveforms, and geodetic data. The estimated seismic moment and maximum slip are $7.5 \times 10^{20}$ Nm ($M_w$ 7.9) and 7.3 m, respectively. The total source duration is approximately 50 s. The derived source model has a unilateral rupture toward the east and a large-slip area north of Kathmandu with the maximum slip. Using the estimated source model together with a one-dimensional (1-D) velocity basin structure model, long-period (> 4 s) ground motions were simulated at a site located in the Kathmandu basin, where strong ground motions with predominant components in a 4–5s period were observed during the 2015 Gorkha earthquake. This simulation demonstrated that the major features of the observed waveforms can be reproduced by our source model and the 1-D basin structure model.

**Keywords:** The 2015 Gorkha earthquake, Source rupture process, Long-period ground motions in the Kathmandu basin, Joint source inversion, Waveform simulation

## Introduction

The 2015 Gorkha earthquake occurred in central Nepal at 11:56 on April 25, 2015, local time (06:11 on April 25, Coordinated Universal Time). The moment magnitude ($M_w$) estimated from the centroid moment tensor (CMT) inversion by the Global CMT (GCMT) Project was 7.9. Based on the source mechanism and hypocenter, this event was a thrust-type interplate earthquake between the subducting Indian plate and the overriding Eurasian plate. This earthquake caused strong ground motions across Nepal with a maximum seismic intensity of VIII on the modified Mercalli intensity scale. This earthquake and the following aftershocks killed approximately 9000 people and injured more than 23,000 people. It was the worst natural disaster to strike Nepal since the 1934 Nepal-Bihar earthquake.

* Correspondence: hkubo@bosai.go.jp
National Research Institute for Earth Science and Disaster Prevention, 3-1, Tennodai, Tsukuba, Ibaraki 305-0006, Japan

The source process of the 2015 Gorkha earthquake has been investigated using various datasets such as near-field waveforms, teleseismic waveforms, and geodetic data (e.g., Avouac et al. 2015; Galetzka et al. 2015; Grandin et al. 2015; Kobayashi et al. 2015; Yagi and Okuwaki 2015). In general, the resolution of source inversion with near-field waveforms (strong ground motion data or high-rate Global Positioning System (GPS) data) is spatially and temporally high because the near-field waveforms are expected to contain much information on the detailed source process. However, in the case of the 2015 Gorkha earthquake, the distribution of near-field stations was one-sided against the source region and this distribution is expected to reduce the source-inversion resolution or bias the solution. On the other hand, teleseismic stations are globally distributed and teleseismic data have a good azimuthal coverage, although the source-inversion resolution of teleseismic waveforms is generally lower than that of

near-field waveforms (e.g., Yokota et al. 2011). Additional use of geodetic data (static displacements) together with waveform data makes the source inversion more stable (e.g., Wald and Graves 2001). Previous studies have shown that a more reliable source model can be obtained by using combined datasets in the source inversion (e.g., Yoshida and Koketsu 1990; Wald and Heaton 1994; Kubo and Kakehi 2013). In this study, therefore, we developed a reliable source model of the 2015 Gorkha earthquake jointly using near-field waveforms, teleseismic waveforms, and geodetic data.

During the 2015 Gorkha earthquake, strong ground motions with predominant components in a 4–5s period were observed in the Kathmandu basin, and the waveform comparison between rock and basin sites has shown that one cause of the characteristic waveforms is the site effect of the Kathmandu basin (Galetzka et al. 2015; Dhakal et al. 2016). The ground motions are also attributed to be the source effect because the 4–5s period components were predominant in the observed spectra even at the rock site (Fig. 3 in Galetzka et al. 2015). Thus, for understanding the long-period ground motions in the Kathmandu basin during this earthquake, both source and site effects should be considered. In this study, we investigated how well the long-period ground motions can be reproduced by the source model estimated from the source inversion and an available one-dimensional (1-D) underground velocity structure model for the Kathmandu basin. Although the source models of the 2015 Gorkha earthquake have been proposed (e.g., Avouac et al. 2015; Galetzka et al. 2015; Grandin et al. 2015; Kobayashi et al. 2015; Yagi and Okuwaki 2015), the waveform simulation in the Kathmandu basin using the derived source model has never been conducted.

In this study, we first estimated the source process of this event using the kinematic joint earthquake source inversion with near-field waveforms, teleseismic waveforms, and geodetic data. Using the derived source model, we investigated the relationships among fault parameters of the characterized source model of the 2015 Gorkha earthquake and compared them with empirical relationships for interplate earthquakes. Because there were few interplate earthquakes in the Himalayan region observed by the modern seismic observation network, it is important to examine whether the 2015 Gorkha earthquake obeys the previous empirical relationships of fault parameters. Then, we discussed its relationship with the interplate-coupling distribution, seismic activity, and past large events. Finally, using the estimated source model together with the 1-D velocity structure model for the Kathmandu basin, we carried out the waveform simulation of long-period (> 4 s) ground motions at a site located in the Kathmandu basin.

## Methods

The source process was estimated by the fully Bayesian multiple-time-window source inversion (Kubo et al. 2016). One advantage of this method is that the distributions of model parameters and hyperparameters (e.g., relative weight of smoothing constraint) produced by the fully Bayesian source inversion are useful in evaluating the uniqueness and reliability of a derived model. Another advantage is that when a non-negative constraint is used, the fully Bayesian source inversion can determine appropriate hyperparameters, whereas a conventional source inversion might not do well. The spatiotemporal smoothing and non-negative constraints for slips were applied following the procedure proposed by Kubo et al. (2016) to obtain a physically reasonable and stable solution. In the source process analysis, we assumed a single rectangular fault model (140 km along the strike × 80 km along the strike, Fig. 1a) with the 293° strike angle referring to the GCMT solution. The dip angle of the fault model was set to 5° to minimize the data-fit residual. The fault model was divided into 160 subfaults of 10 km × 10 km. Because we estimated the weights of the two orthogonal slips for each time window at each subfault under the non-negative constraint, the rake angle of the slip vector for each subfault was allowed a variation from the central rake angle of ±45°. The central rake angle of 108° referred to the GCMT solution. The horizontal location of the rupture starting point was fixed at the epicenter determined by the Nepal Seismological Centre (NSC) (84.75° E, 28.24° N). The depth of the rupture starting point was set to 8 km based on the fit of near-field waveforms. The slip time history at each subfault was represented by a series of six smoothed-ramp functions with a 4.0-s width, each with a 2.0-s lag. The triggering velocity of the first time window of 3.4 km/s was selected to minimize the data-fit residual. Although the amplitudes of the near-field and teleseismic waveforms in the source inversion were normalized by the maximum amplitude at each station, the normalization at each station was not applied to the geodetic data to avoid the instability caused by the low signal-to-noise ratio data with small absolute values (Wald and Graves 2001). The relative weights among the datasets were determined so that the data fit for each dataset is satisfactory.

For near-field waveforms, we used three components of 5-Hz GPS waveforms at five stations produced by Galetzka et al. (2015) (Fig. 1a). Although Galetzka et al. (2015) also produced the waveforms at the Nepal Academy of Science and Technology (NAST) station (Fig. 1a), we did not use this data because NAST is located in the Kathmandu basin and its waveform data were expected to be significantly amplified and delayed by the effect of the Kathmandu basin. The observed displacement waveforms were numerically differentiated into velocity in the time

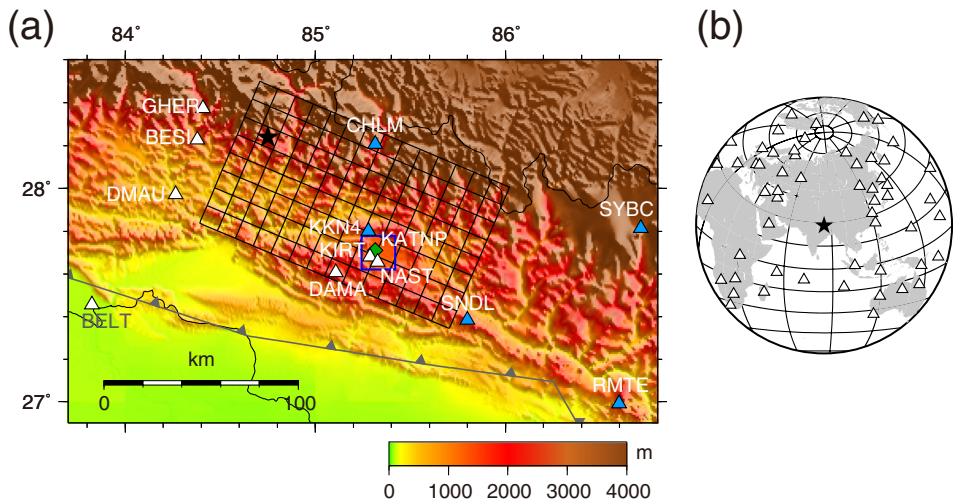


**Fig. 1** **a** Station map of near-field waveforms and geodetic data. *Blue triangles* represent the 5-Hz GPS stations, from which waveforms and static displacements were used. *White triangles* represent the low-rate GPS stations, from which static displacements were used. *Green diamond* represents the KATNP station. *Blue open square* indicates the rough location of Kathmandu. *Black star* represents the rupture starting point. *Black squares* represent the subfaults of the assumed fault model. *Gray line* indicates the surface intersection of the Indian and Eurasian plates (Bird 2003). *Background color* indicates the land height above sea level. **b** Station map of teleseismic data (*open triangles*). *Black star* represents the rupture starting point

domain and were band-pass filtered from 4 to 50 s. The time length of the near-field waveforms is 50–60 s, which depends on the record length at each station (starting 10 s before theoretical S-wave arrival). Green's functions of near-field waveforms were calculated using the discrete wave number method (Bouchon 1981) and the reflection/transmission matrix method (Kennett and Kerry 1979) assuming a 1-D velocity structure model. The 1-D velocity structure model was constructed based on Monsalve et al. (2006), who developed 1-D velocity structure models in east Nepal and south Tibet to relocate earthquakes in these regions.

For teleseismic waveforms, we used P-wave parts of vertical-component broadband waveforms at 45 stations of the Global Seismograph Network (GSN) (Fig. 1b). The instrumental responses were deconvolved from the original recordings to obtain the ground velocities. The observed velocity waveforms were numerically integrated into displacement in the time domain, were band-pass filtered from 4 to 50 s, and were resampled at 5 Hz. The time length of the teleseismic waveforms is 110 s (starting 10 s before P-wave arrival, which was carefully identified by visual inspection). Green's functions of teleseismic body waves were calculated using the program package of Kikuchi and Kanamori (2004) with the 1-D source velocity structure model (Monsalve et al. 2006).

For geodetic data, we used three components of static displacements at 12 stations produced by Galetzka et al. (2015) (Fig. 1a). Considering the difference in observation error between horizontal and vertical components, the relative weight of the vertical component against the horizontal component was set to 0.5. For Green's functions of static displacements, we calculated the theoretical static displacements by a unit slip on each subfault assuming a homogeneous elastic half-space, as proposed in Okada (1992).

## Results and discussion

### Source model of the 2015 Gorkha earthquake

From the posterior probability distributions for slips at each subfault on each time window, which were based on the 80,000 ensembles of a source model produced by the fully Bayesian multiple-time-window source inversion (Kubo et al. 2016), we obtained the optimal source model composed of median slips of their distributions. The seismic moment and maximum slip of the estimated source model of the 2015 Gorkha earthquake are $7.5 \times 10^{20}$ Nm ($M_w$ 7.9) and 7.3 m, respectively. Figure 2 shows the final-slip distribution. Figure 3 shows the rupture progression and slip rate function at each subfault. The rupture of the 2015 Gorkha earthquake was unilateral toward the east. A large-slip (> 4 m) area with the maximum slip was found north of Kathmandu (from 60 to 100 km east-southeast of the hypocenter). In addition, the other relatively large-slip areas were located west-northwest of Kathmandu (from 40 to 50 km southeast of the hypocenter) and 20 km southeast of Kathmandu. In the first 10 s, the rupture grew around the hypocenter. After 10 s, the rupture started to propagate toward the east. From 10 to 20 s, the rupture mainly propagated in the relatively shallow region, west of Kathmandu.

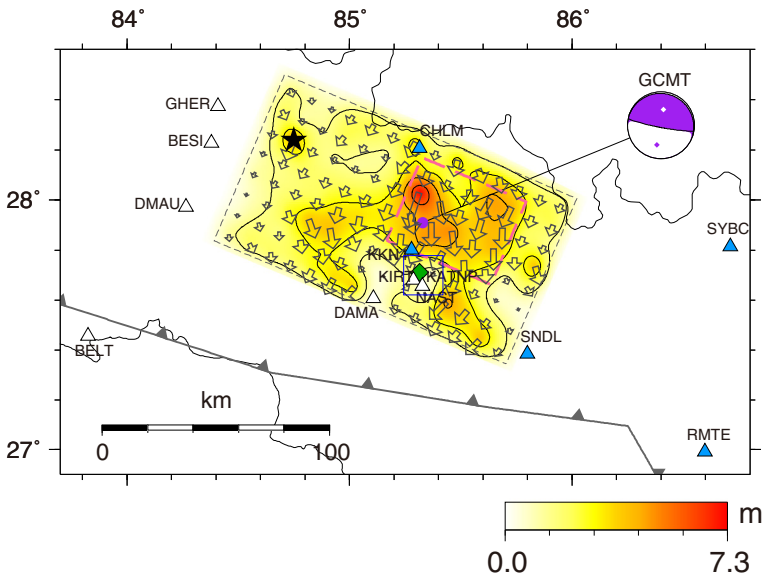


**Fig. 2** Map projection of the final-slip distribution. Contour interval is 1.46 m. *Arrows* indicate the slip amplitude and direction of the hanging wall relative to the foot wall. *Black star* indicates the rupture starting point. *Broken rectangle* represents the assumed fault model. *Broken pink rectangle* represents the estimated asperity. Focal mechanism represents the GCMT solution of the 2015 Gorkha earthquake

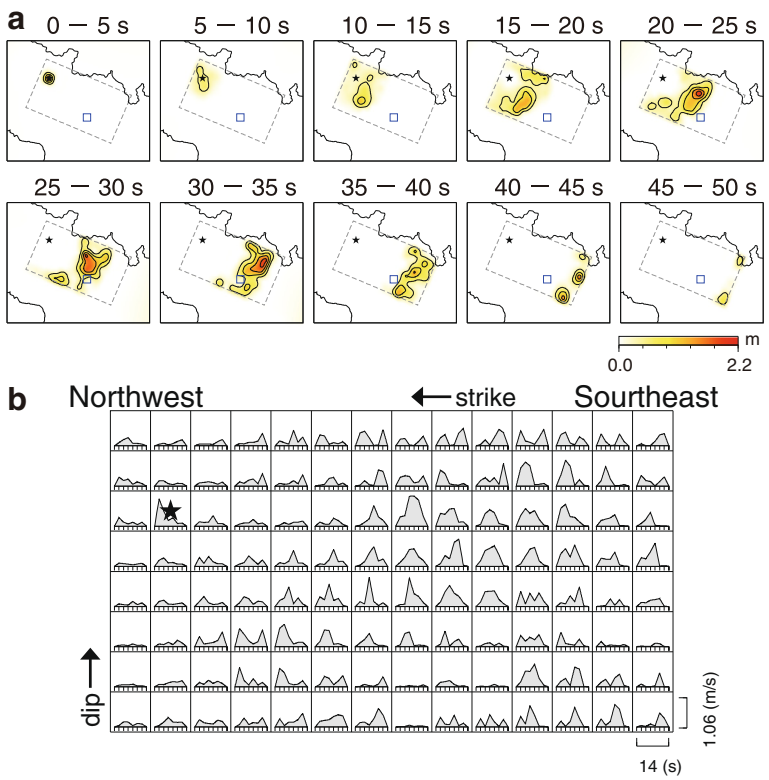


**Fig. 3 a** Snapshots of the rupture progression at a time step of 5 s. Slip contour is 0.44 m. *Black star* indicates the rupture starting point. *Broken rectangle* represents the assumed fault model. **b** Slip rate function at each subfault. *Black star* represents the subfault corresponding to the rupture starting point

Then, from 20 to 35 s, the rupture with large slips propagated in the relatively deep region, north of Kathmandu. The total source duration was approximately 50 s.

The variance reductions of near-field waveforms, teleseismic waveforms, and geodetic data are 86.3, 62.7, and 99.6 %, respectively. The synthetics from the obtained source model match the observations very well (Figs. 4 and 5).z

### Fault parameters of the characterized source model

Murotani et al. (2008) proposed empirical relationships for the characterized source models of large interplate earthquakes in Japan, and Murotani et al. (2013) demonstrated that the empirical relationships of Murotani et al. (2008) are applicable even to giant ($M \approx 9$) interplate earthquakes. Here, we characterized the heterogeneous final-slip distribution of our source model following the procedure of Somerville et al. (1999) (Table 1) and compared the fault parameter relationships of the 2015 Gorkha earthquake with the relationships of other interplate events and the empirical relationships for interplate earthquakes (Murotani et al. 2008) (Fig. 6). Figure 6 shows that the fault parameters

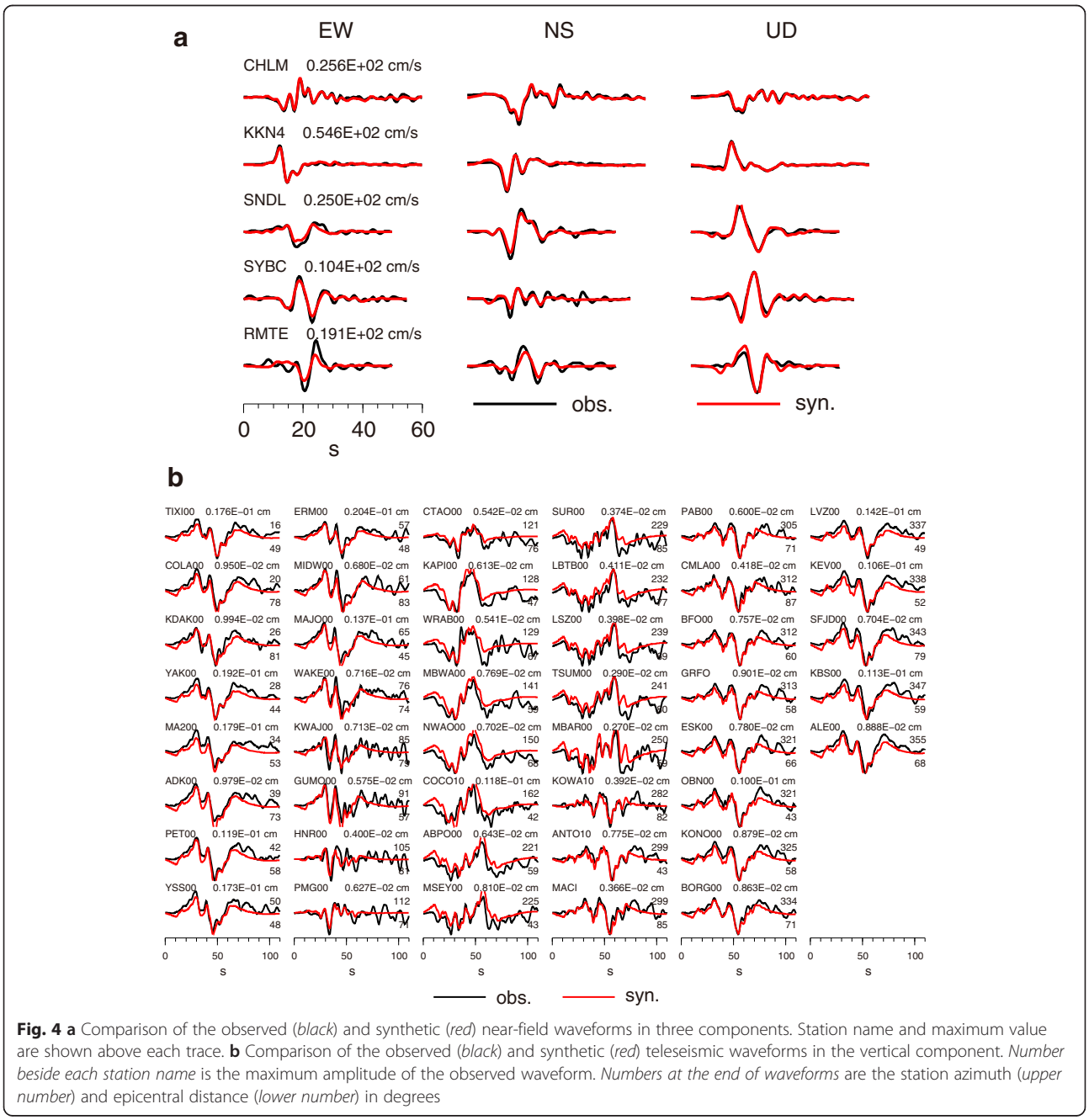


**Fig. 4** **a** Comparison of the observed (*black*) and synthetic (*red*) near-field waveforms in three components. Station name and maximum value are shown above each trace. **b** Comparison of the observed (*black*) and synthetic (*red*) teleseismic waveforms in the vertical component. *Number beside each station name* is the maximum amplitude of the observed waveform. *Numbers at the end of waveforms* are the station azimuth (*upper number*) and epicentral distance (*lower number*) in degrees

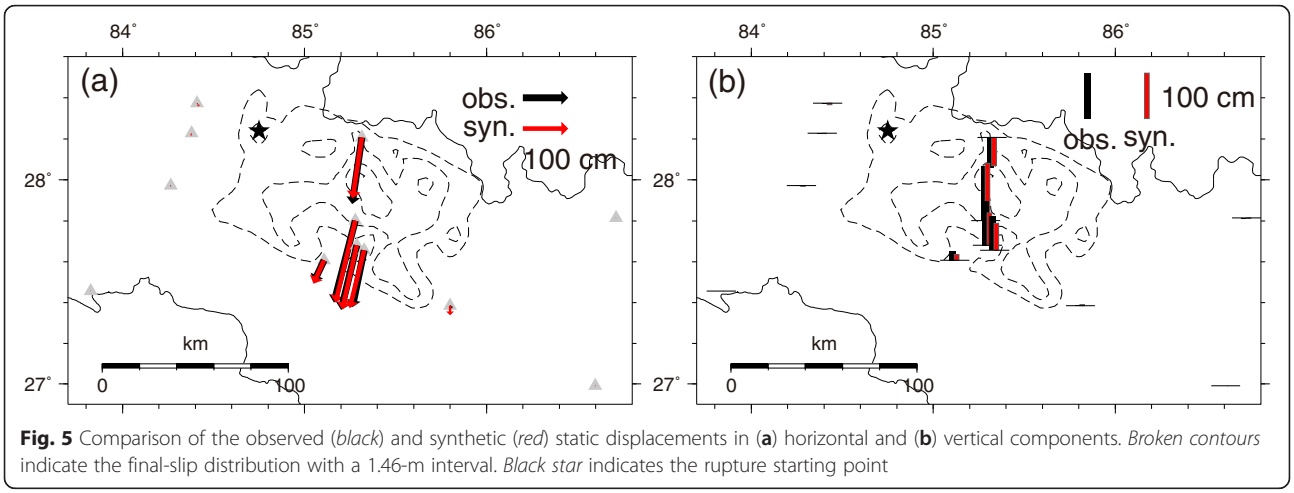


**Fig. 5** Comparison of the observed (*black*) and synthetic (*red*) static displacements in (**a**) horizontal and (**b**) vertical components. *Broken contours* indicate the final-slip distribution with a 1.46-m interval. *Black star* indicates the rupture starting point

of the 2015 Gorkha earthquake are consistent with the previous empirical relationships for interplate earthquakes. This means that the 2015 Gorkha earthquake was a standard interplate earthquake as far as the fault parameter scaling is considered. The asperity region was located north of Kathmandu (Fig. 5), which corresponds to the centroid location of the GCMT.

### Relationship with interplate-coupling distribution, seismic activity, and past large events

In the Himalayan continental collision region, a belt of microseismicity has been observed (e.g., Pandey et al. 1995, 1999), which corresponds to the creeping-locked transition (e.g., Ader et al. 2012). From the microseismicity belt to the surface, the Main Himalayan thrust fault is considered to be fully coupled and it has been predicted that large interplate earthquakes will occur (e.g., Bilham et al 1997; Ader et al. 2012). In Fig. 7, the source model of the 2015 Gorkha earthquake is compared with the interseismic coupling distribution (Ader et al. 2012), the microseismicity distribution before the mainshock (Ader et al. 2012), and the aftershock distribution determined by the NSC. This figure shows that the north part of the rupture area of the 2015 Gorkha earthquake overlapped the microseismicity and the aftershocks. Figure 7 also shows that most of the rupture was located in the high-coupling-ratio region (> 0.8).

Nepal has been struck by many large earthquakes, such as the 1505 West Nepal earthquake ($M_w \approx 8.2$), the 1833 Mid-Nepal earthquake ($M_w \approx 7.6$), and the 1934 Nepal-Bihar earthquake ($M_w \approx 8.1$). Considering the inferred source regions of these events (e.g., Bilham 1995; Ambraseys and Douglas 2004; Sapkota et al. 2013), the rupture area of the 2015 event seems to overlap the source region of the 1833 event (Fig. 7). Given that the convergence rate in central and eastern Nepal is 17.8 mm/year (Ader et al. 2012) and that this region has been coupled for 182 years at a coupling ratio of 0.8, the accumulated slip deficit at the time of the 2015 event was expected to be approximately 2.6 m. This value is comparable to the estimated average slip of 2.5 m for the 2015 Gorkha earthquake (Table 1), which suggests the possibility that the 2015 event was the reactivation of the preexisting asperity of the 1833 event.

### Waveform simulation in the Kathmandu basin

In the Kathmandu basin, strong ground motions with predominant components in a 4–5s period were observed during the 2015 Gorkha earthquake (Galetzka et al. 2015; Dhakal et al. 2016). Here, we simulated the long-period ground motions using the estimated source model and 1-D velocity structure models. For the observed waveforms in the Kathmandu basin, we used the strong ground motions at Kantipath (KATNP, Fig. 1) recorded by a seismograph maintained by the U.S. Geological Survey (USGS). The calculation method of the synthetics was the same as that of the Green's functions of near-field waveforms. For the 1-D velocity structure model, we used three models (Fig. 8a). M-model is the rock model based on Monsalve et al. (2006) and the same as that used in the calculation of the Green's functions of near-field waveforms. The other models include the structure of the Kathmandu basin. P-model is based on Pandey (2000), who proposed the basin structure

**Table 1** Fault parameters of the characterized source model of the 2015 Gorkha earthquake

| Seismic moment (N*m) | Rupture area ($km^2$) | Average slip (m) | Asperity area ($km^2$) | Average slip of asperity (m) |
|---|---|---|---|---|
| $8.1 \times 10^{20}$ | 11,200 | 2.5 | 2000 | 4.0 |

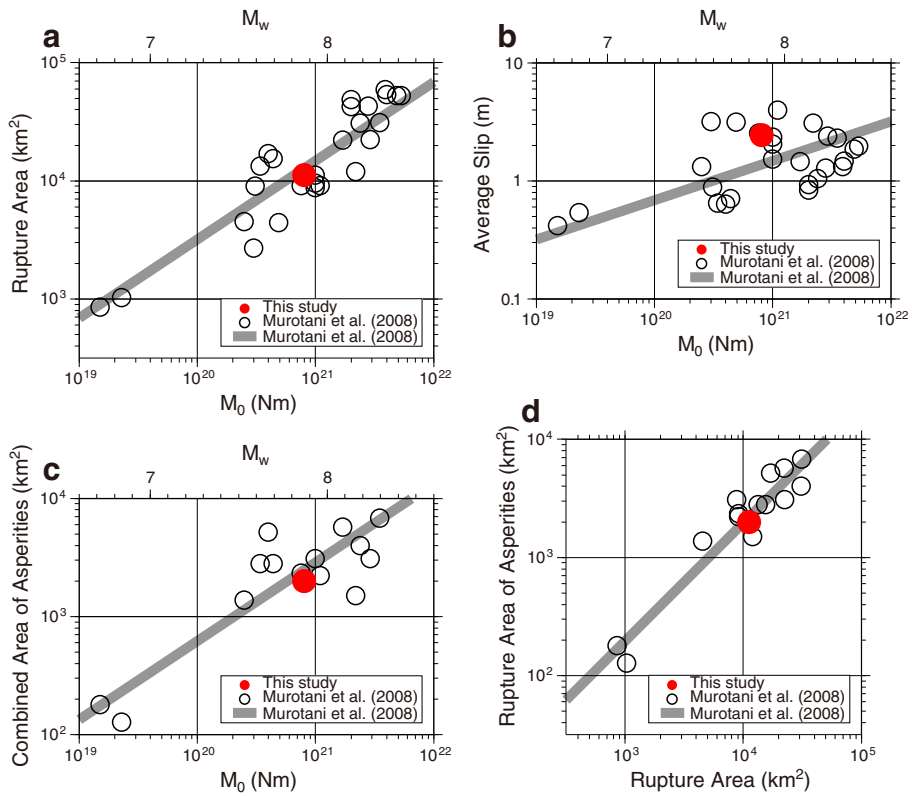


**Fig. 6** Relationship of the (**a**) rupture area, (**b**) average slip, and (**c**) combined area of asperities with seismic moment. **d** Relationship between the combined area of asperities and rupture area. *Open circles* represent the interplate earthquakes listed in Murotani et al. (2008). *Red closed circles* represent the 2015 Gorkha earthquake. *Gray lines* represent the empirical scaling relationships of the interplate earthquakes proposed by Murotani et al. (2008)

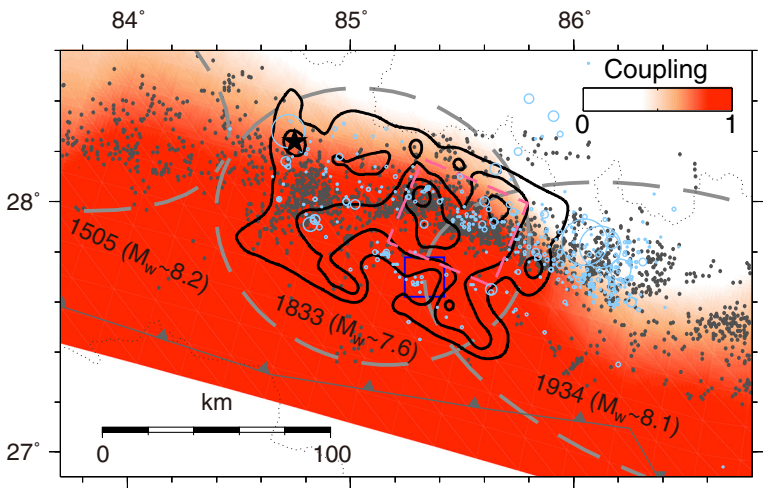


**Fig. 7** Comparison of the source model of the 2015 Gorkha earthquake (*black contours* with a 1.46-m interval) with interseismic coupling distribution (*shades of red*, Ader et al. 2012), midcrustal microseismicity from 1996 to 2008 (*gray dots*, Ader et al. 2012), and aftershock distribution to September 30, 2015, determined by NSC (*sky blue circles*). *Gray broken ellipses* show the rough locations of the 1505 West Nepal earthquake ($M_w \approx 8.2$), the 1983 Mid-Nepal earthquake ($M_w \approx 7.6$), and the 1934 Nepal-Bihar earthquake ($M_w \approx 8.1$). The moment magnitude values shown were determined by Ambraseys and Douglas (2004)

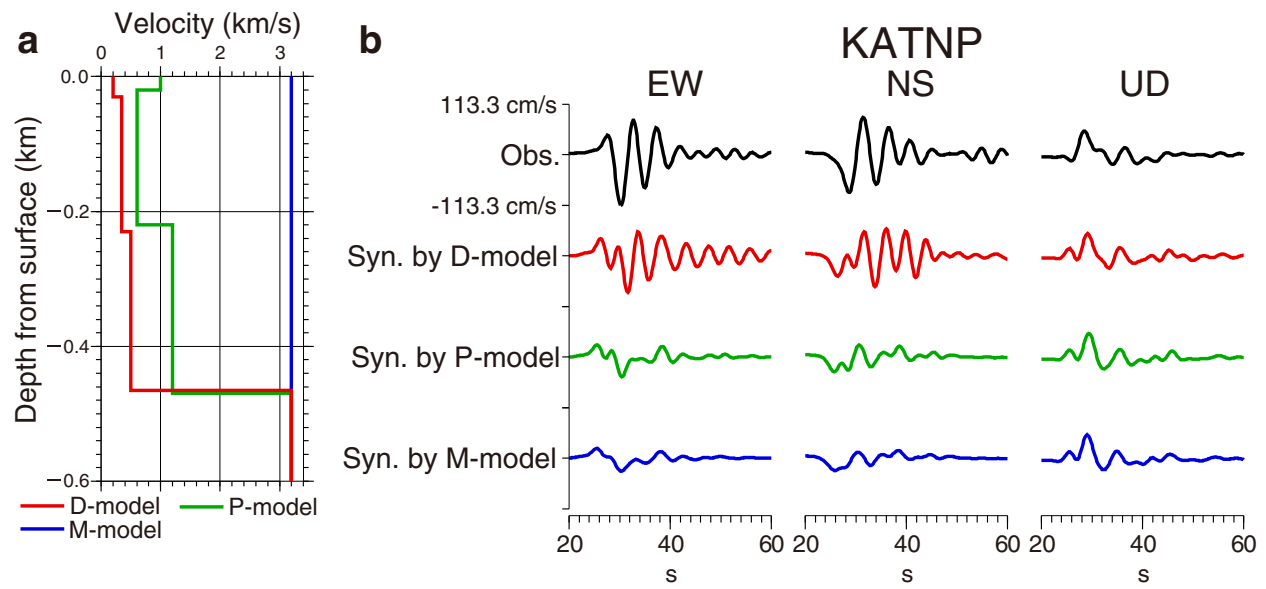


**Fig. 8 a** One-dimensional shear velocity models from surface to 0.6-km depth. D-model (*red*), P-model (*green*), and M-model (*blue*) were based on Dhakal et al. (2016), Pandey (2000), and Monsalve et al. (2006), respectively. **b** Comparison among the observed waveforms at KATNP (*black*) and synthetic waveforms produced by D-model (*red*), P-model (*green*), and M-model (*blue*)

model on the basis of the results of the common-depth-point reflection survey. D-model is based on Dhakal et al. (2016), who inferred the basin structure model from the horizontal-to-vertical spectral ratios of aftershock records at KATNP following the borehole logging and geological data. The velocity values in the basin part of the D-model are lower than those of the P-model.

Figure 8b shows the comparison of the observed velocity waveforms at KATNP with the synthetic waveforms produced by the structure models. These waveforms were band-pass filtered from 4 to 50 s. The horizontal components of the observed waveforms have large amplitudes and long durations as compared to the synthetic waveforms produced by the rock model (M-model). This

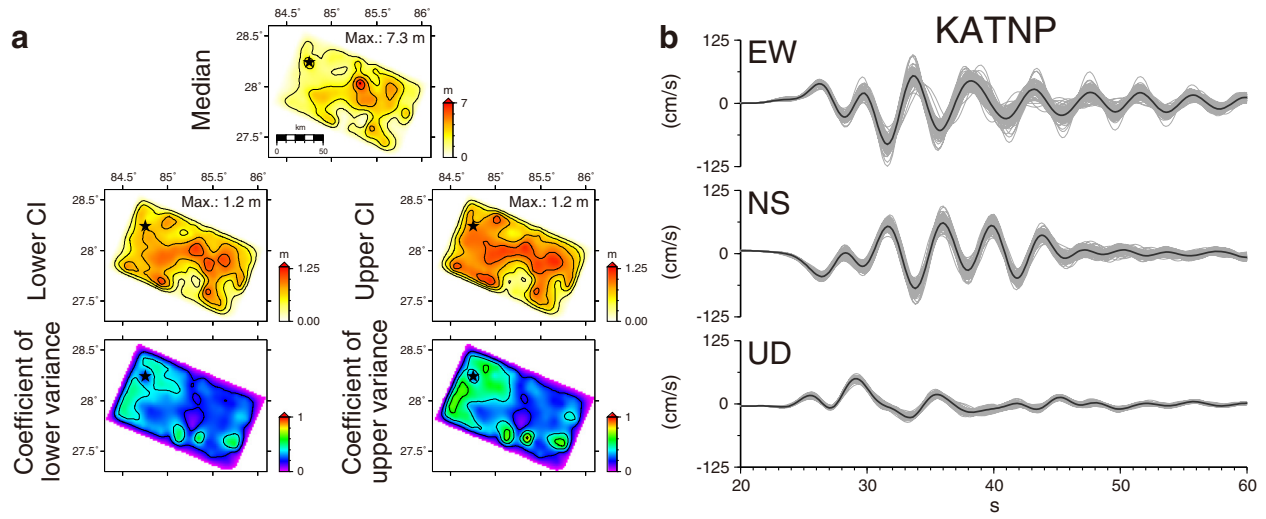


**Fig. 9 a** Distributions of medians, lower credible intervals ([median] – [2.5th percentile]), coefficients of lower variance ([lower credible interval]/[median]), upper credible intervals ([97.5th percentile] – [median]), and coefficients of upper variance ([upper credible interval]/[median]) for final slips. *Black stars* represent the rupture starting point. The contour interval in each figure corresponds to the tick of its color bar. **b** Comparisons of the synthetic waveforms at KATNP produced by the optimal source model (*black*) and synthetic waveforms produced by each source-model sample (*gray*)

difference is presumably caused by the site amplification of the Kathmandu basin. The horizontal components of the synthetic waveforms produced by the P-model have little effect on the basin amplification and are similar to the synthetic waveforms produced by the M-model, but not to the observed waveforms. On the other hand, the horizontal components of the synthetic waveforms produced by the D-model are significantly affected by the basin amplification and are similar to the observed ones. Thus, in the long-period band (> 4 s), the synthetic waveforms produced by the D-model can reproduce the observation much better than those produced by the P-model. We also found that there is little difference in the vertical component among the synthetic waveforms of the three models and that all synthetic vertical-component waveforms are similar to the observed ones. This means that there was little amplification due to the Kathmandu basin in the vertical component of the long-period band (> 4 s).

Moreover, we investigated the uncertainty of our source model and its effect on the result of the waveform simulation, using the posterior probability distributions for slips at each subfault on each time window and the source-model ensembles produced by the fully Bayesian source inversion method (Kubo et al. 2016). Figure 9a shows the final-slip uncertainty of our source model. In the region having median slips of 3 m and more, the credible interval values are at most 1.2 m, and the coefficients of variance are mostly under 0.3. In Fig. 9b, the synthetic waveforms produced by each source-model ensemble are compared with the synthetic waveforms at KATNP produced by the optimal source model (Figs. 2 and 3). Both the waveforms were calculated using the D-model. This figure shows that the variance of the synthetic waveforms is not large among the source-model ensembles. These results indicate that the uncertainty of our source model is not so large and does not largely affect the result of the waveform simulation.

Thus, the waveform simulations demonstrated that the overall feature of the observed long-period ground motions at KATNP can be explained by our source model and the basin structure model of Dhakal et al. (2016). However, some discrepancies between the observed and synthetic waveforms still remain. For example, the polarity of the initial phase of the vertical component differs between the observation and synthetics, and this synthetic phase was mainly generated from the relatively large-slip area west-northwest of Kathmandu. This necessitates further investigations of the source model, particularly the slips west-northwest of Kathmandu. In addition, the waveform simulation in this study was conducted at only one station (KATNP). For further understanding of the generation mechanism of strong ground motions in the Kathmandu basin, it is necessary not only to improve the structure model of the Kathmandu basin, including the development of its 3-D model, but also to further develop the strong-motion seismograph network.

## Conclusions

We estimated the source model of the 2015 Gorkha earthquake using the joint source inversion with near-field waveforms, teleseismic body waves, and geodetic data. The estimated seismic moment and maximum slip are $7.5 \times 10^{20}$ Nm ($M_w$ 7.9) and 7.3 m, respectively. The derived source model has the unilateral rupture toward the east and a large-slip area north of Kathmandu with the maximum slip. Then, we investigated the relationships among the fault parameters of the characterized source model of the 2015 Gorkha earthquake and found that the fault parameter relationships of this earthquake are consistent with the previous empirical relationships of interplate earthquakes. The comparison of the final-slip distribution of this earthquake with the interplate-coupling distribution, seismic activity, and past large events indicated that the 2015 event could be the reactivation of the preexisting asperity of the 1833 Mid-Nepal earthquake. Using the estimated source model together with the 1-D velocity structure model of the Kathmandu basin, we simulated the long-period (> 4 s) ground motions at KATNP located in the Kathmandu basin. The waveform simulation demonstrated that the major features of the observation can be reproduced by our source model and the 1-D basin structure model of Dhakal et al. (2016).

#### Competing interests

The authors have no competing interests to declare.

#### Authors' contributions

HK analyzed the data, interpreted the results, carried out the waveform simulations, and drafted the manuscript. YD and WS participated in the study design and the interpretation of the results. TK, SA, and HF participated in the study design. All authors read and approved the final manuscript.

#### Acknowledgements

We thank Prof. Kazuki Koketsu and the anonymous reviewer for their helpful comments. The Department of Mines and Geology, Tribhuvan University, and California Institute of Technology are acknowledged for providing us with high-rate GPS data. Strong-motion data observed by the USGS were gathered from the Center for Engineering Strong Motion Data. Teleseismic data observed by the GSN were collected from the Data Management Center of Incorporated Research Institutions for Seismology. The CMT solution estimated by the GCMT Project and hypocenter information estimated by the NSC were used. Topographic data were obtained from the Geographic Information Network of Alaska. Generic Mapping Tools (Wessel and Smith 1998) were used to draw the figures.

Received: 30 October 2015 Accepted: 21 January 2016
Published online: 05 February 2016

#### References

Ader T, Avouac JP, Liu-Zeng J, Lyon-Caen H, Bollinger L, Galetzka J, Genrich J, Thomas M, Chanard K, Sapkota SN, Rajaure S, Shrestha P, Ding L, Flouzat M (2012) Convergence rate across the Nepal Himalaya and interseismic coupling on the Main Himalayan Thrust: implications for seismic hazard. J Geophys Res 117(B4):B04403. doi:10.1029/2011JB009071

Ambraseys NN, Douglas J (2004) Magnitude calibration of north Indian earthquakes. Geophys J Int 159(1):165–206. doi:10.1111/j.1365-246X.2004.02323.x

Avouac JP, Meng L, Wei S, Wang T, Ampuero JP (2015) Lower edge of locked Main Himalayan Thrust unzipped by the 2015 Gorkha earthquake. Nat Geosci 8:708–711. doi:10.1038/ngeo2518

Bilham R (1995) Location and magnitude of the 1833 Nepal earthquake and its relation to the rupture zones of contiguous great Himalayan earthquakes. Curr Sci 69(2):25

Bilham R, Larson K, Freymueller J (1997) GPS measurements of present-day convergence across the Nepal Himalaya. Nature 386:61–64. doi:10.1038/386061a0

Bird P (2003) An updated digital model of plate boundaries. Geochem Geophys Geosyst 4(3):1027. doi:10.1029/2001GC000252

Bouchon M (1981) A simple method to calculate Green's function for elastic layered media. Bull Seismol Soc Am 71(4):959–971

Dhakal YP, Kubo H, Suzuki W, Kunugi T, Aoi S, Fujiwara H (2016) An analysis of strong ground motion and site amplification at Kantipath, Kathmandu from the 2015 Mw 7.8 Gorkha Earthquake, Nepal and its aftershocks. Earth Planets Space (submitted).

Galetzka J, Melgar D, Genrich JF, Geng J, Owen S, Lindsey EO, Xu X, Bock Y, Avouac JP, Adhikari LB, Upreti BN, Pratt-Sitaula B, Bhattarai TN, Sitaula BP, Moore A, Hudnut KW, Szeliga W, Normandeau J, Fend M, Flouzat M, Bollinger L, Shrestha P, Koirala B, Gautam U, Bhatterai M, Gupta R, Kandel T, Timsina C, Sapkota SN, Rajaure S, Maharjan N (2015) Slip pulse and resonance of Kathmandu basin during the 2015 Mw 7.8 Gorkha earthquake, Nepal imaged with geodesy. Science 349(6252):1091–1095. doi:10.1126/science.aac6383

Grandin R, Vallée M, Satriano C, Lacassin R, Klinger Y, Simoes M, Bollinger L (2015) Rupture process of the $M_W = 7.9$ 2015 Gorkha earthquake (Nepal): insights into Himalayan megathrust segmentation. Geophys Res Lett 42(20):8373–8382. doi:10.1002/2015GL066044

Kennett BLN, Kerry NJ (1979) Seismic waves in a stratified half space. Geophys J R Astr Soc 57:557–583

Kikuchi M, Kanamori H (2004) Note on teleseismic body-wave inversion program. http://www.eri.u-tokyo.ac.jp/ETAL/KIKUCHI/. Accessed 28 Jan 2015.

Kobayashi T, Morishita Y, Yarai H (2015) Detailed crustal deformation and fault rupture of the 2015 Gorkha earthquake, Nepal, revealed from ScanSAR-based interferograms of ALOS-2. Earth Planets Space 67:201. doi:10.1186/s40623-015-0359-z

Kubo H, Kakehi Y (2013) Source process of the 2011 Tohoku earthquake estimated from the joint inversion of teleseismic body waves and geodetic data including seafloor observation data: source model with enhanced reliability by using objectively determined inversion settings. Bull Seismol Soc Am 103(2B):1195–1220. doi:10.1785/0120120113

Kubo H, Asano K, Iwata T, Aoi S (2016) Development of fully Bayesian multiple-time-window source inversion. Geophys J Int 204(3):1601–1619 doi:10.1093/gji/ggv540.

Monsalve G, Sheehan A, Schulte-Pelkum V, Rajaure S, Pandey MR, Wu F (2006) Seismicity and one-dimensional velocity structure of the Himalayan collision zone: earthquakes in the crust and upper mantle. J Geophys Res 111(B10), B10301. doi:10.1029/2005JB004062

Murotani S, Miyake H, Koketsu K (2008a) Scaling of characterized slip models for plate-boundary earthquakes. Earth Planets Space 60:987–991

Murotani S, Satake K, Fujii Y (2008b) Scaling relations of seismic moment, rupture area, average slip, and asperity size for $M \sim 9$ subduction-zone earthquakes. Geophys Res Lett 40(19):5070–5074. doi:10.1002/grl.50976

Okada Y (1992) Internal deformation due to shear and tensile faults in a half-space. Bull Seismol Soc Am 82(2):1018–1040

Pandey MR (2000), Ground response of Kathmandu valley on the basis of microtremors, Paper. Proceedings of the 12th World Conference on Earthquake Engineering, Auckland, New Zealand, 30 Jan 4 – Feb 2000, Paper No. 2106.

Pandey MR, Tankudar RP, Avouac JP, Lavé J, Massot JP (1995) Interseismic strain accumulation on the Himalayan crustal ramp (Nepal). Geophys Res Lett 22(7): 751–754

Pandey MR, Tankudar RP, Avouac JP, Vergne J, Héritier T (1999) Seismotectonics of the Nepal Himalaya from a local seismic network. J Asian Earth Sci 17:703–712

Sapkota SN, Bollinger L, Klinger Y, Tapponnier P, Gaudemer Y, Tiwari D (2013) Primary surface ruptures of the great Himalayan earthquakes in 1934 and 1255. Nat Geosci 6:71–76. doi:10.1038/ngeo1720

Somerville PG, Irikura K, Graves R, Sawada S, Wald D, Abrahamson N, Iwasaki Y, Kagawa T, Smith N, Kowada A (1999) Characterizing crustal earthquake slip models for the prediction of strong ground motion. Seismol Res Lett 70(1):59–80

Wald DJ, Heaton TH (1994) Spatial and temporal distribution of slip for the 1992 Landers, California, earthquake. Bull Seismol Soc Am 84(3):668–691

Wald DJ, Graves RW (2001) Resolution analysis of finite fault source inversion using one- and three-dimensional Green's functions 2. Combining seismic and geodetic data. J Geophys Res 106(B5):8767–8788. doi:10.1029/2000JB900435

Wessel P, Smith WHF (1998) New, improved version of Generic Mapping Tools released. EOS Trans Am geophys Un 79:579

Yagi Y, Okuwaki R (2015) Integrated seismic source model of the 2015 Gorkha, Nepal, earthquake. Geophys Res Lett 42(15):6229–6235. doi:10.1002/2015GL064995

Yokota Y, Koketsu K, Fujii Y, Satake K, Sakai S, Shinohara M, Kanazawa T (2011) Joint inversion of strong motion, teleseismic, geodetic, and tsunami datasets for the rupture process of the 2011 Tohoku earthquake. Geophys Res Lett 38(7):L00G21. doi:10.1029/2011GL050098

Yoshida S, Koketsu K (1990) Simultaneous inversion of waveform and geodetic data for the rupture process of the 1984 Naganoken-Seibu, Japan, earthquake. Geophys J Int 103(2):355–362